

Modeling Charge Transport in C_{60} -based Self-assembled Monolayers for Applications in Field-Effect Transistors

S. Leitherer,¹ C. M. Jäger,² M. Halik,³ T. Clark,² and M. Thoss¹

¹⁾*Institute for Theoretical Physics and Interdisciplinary Center for Molecular Materials,*

University Erlangen-Nürnberg,

Staudtstr. 7/B2, D-91058 Erlangen, Germany

²⁾*Computer-Chemie-Centrum and Interdisciplinary Center for Molecular Materials,*
University Erlangen-Nürnberg,

Nügelsbachstr. 25, 91052 Erlangen, Germany

³⁾*Organic Materials & Devices, Institute of Polymer Materials,*
Department of Materials Science,

University Erlangen-Nürnberg,

Martensstr. 7, D-91058 Erlangen, Germany

(Dated: 9 November 2018)

We have investigated the conductance properties of C_{60} -containing self-assembled monolayers (SAMs), which are used in organic field-effect transistors, employing a combination of molecular-dynamics simulations, semiempirical electronic structure calculations and Landauer transport theory. The results reveal the close relation between the transport characteristics and the structural and electronic properties of the SAM. Furthermore, both local pathways of charge transport in the SAMs and the influence of structural fluctuations are analyzed.

I. INTRODUCTION

Field-effect transistors (FETs) with thin films of organic π -conjugated materials as active semiconductor have developed towards a serious alternative for low-cost and flexible electronics on large areas.^{1,2} The fact that charge transport in those organic films occurs essentially in the first molecular monolayer in close proximity to the dielectric interface^{3,4} makes a self-assembled monolayer field-effect transistor (SAMFET) a perfect device for studying charge-carrier transport properties in organic materials.⁵ In SAMFETs, the active π -system is linked to a flexible insulating alkyl-chain that is covalently bound to a suitable surface. Thus, the π -systems form an almost 2D confined transport channel on molecular scale in thickness^{6,7} and the n-alkyl linkers compose a hybrid gate dielectric together with the insulating anchor oxide (AlO_x).⁸ Hole and electron transport have been demonstrated in SAMFETs making the concept a veritable approach in molecular scale electronics.^{6,7,9,10}

The experimental advances have triggered theoretical studies of charge transport in organic thin films within the context of SAMFETs.^{5,11} The theoretical description of charge transport in these systems involves the principle problem of accounting for structural flexibility and inhomogeneity. Thus, the characterization of the electronic structure must be combined with conformational sampling, which in view of the complexity of the systems, represents a significant challenge. Furthermore, the mechanism of electron transport is *a priori* not obvious. While dephasing due to both structural fluctuations and inelastic processes may favor hopping-type transport at higher temperatures, band-type coherent transport can also contribute, in particular in systems with stronger intermolecular coupling and at lower temperatures.

In previous work, some of the authors investigated charge transport in C_{60} -based SAMs using a combination of molecular-dynamics (MD) simulation, semiempirical electronic structure calculations and Monte Carlo (MC) transport studies.¹¹ In agreement with experimental results,^{12,13} the study revealed the crucial influence of the morphology of the SAM on the transport properties. In the present paper, we extend the previous study using a fully quantum mechanical description of transport. Specifically, we employ Landauer transport theory,¹⁴ which provides a coherent transport treatment based on elastic scattering mechanisms and is thus complementary to the MC-based investigations in Ref. 11. Moreover, we use the theory of local currents¹⁵ to investigate pathways of electron transport in the SAM

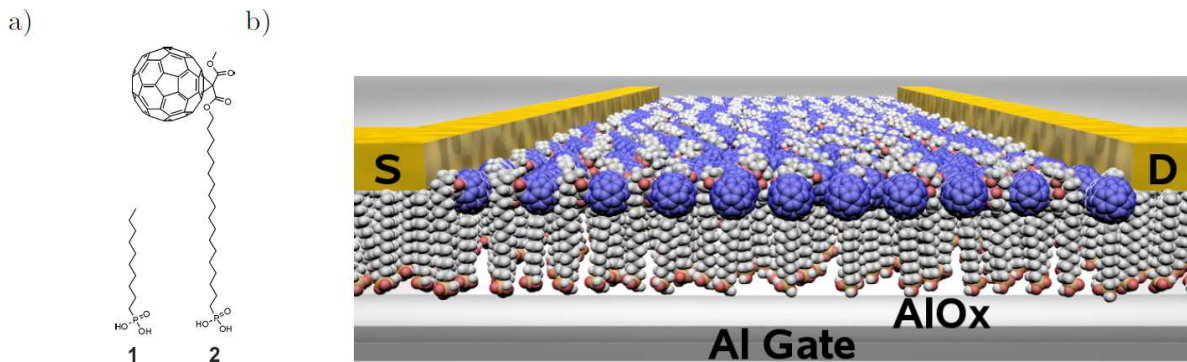


FIG. 1. Schematic and chemical composition of SAMFET devices. (a) Chemical structure of the SAM forming phosphonic acids C_{10} -PA (**1**) and C_{60} - C_{18} -PA (**2**). (b) Schematic SAMFET setup with Au source and drain electrodes, and AlO_x gate dielectric between SAM and an Al gate.

and study the influence of structural fluctuations on the transport properties.

The article is organized as follows: In Sec. IIA, we introduce the SAMFET devices containing the layers of organic molecules, which are investigated throughout the paper. The theoretical methodology is outlined in Sec. IIB - IID, including MD simulations, electronic structure calculations, the Landauer transport approach and the theory of local currents. In Sec. III, the results of the simulations obtained for various SAMs, which differ in their structural properties, are presented. In particular, we discuss the electronic structure and the transport properties and their relation to the morphology of the SAMs. In addition, local pathways for charge transport in the SAMs are investigated and the influence of structural fluctuations on the transport properties of the SAMs is analyzed.

II. SYSTEMS AND METHODS

The theoretical methodology employed to simulate charge transport in SAMs involves three steps: (i) a characterization of the structure of the SAMs with MD simulations, (ii) a determination of the electronic structure using semiempirical molecular orbital (MO) theory, and (iii) transport calculations within Landauer theory. In the following, the different methods are described. We begin with a brief introduction of the systems investigated and their use in SAMFET devices.

A. Setup

A scheme of the self-assembled monolayer field-effect transistor (SAMFET) device and its chemical composition is shown in Fig. 1. The SAM is formed by fullerene-functionalized octadecyl-phosphonic acids (PAs) (in the following denoted by C_{60} - C_{18} -PA) and C_{10} -PA in various stoichiometric ratios. The SAM is separated from the aluminum gate electrode at the bottom by an AlO_x layer, which together with the alkyl chains of the SAM builds the dielectric of the device.¹⁶ Lithographically patterned gold (30 nm) is placed on top of the SAM, serving as source and drain electrodes.¹¹ The semiconducting C_{60} head groups of the functionalized PA in the SAM form the active transistor channel in the device. In this paper, we focus on the modeling of charge transport within the SAM. Therefore, the influence of a gate potential and the AlO_x layer is not taken into account. The coupling to the gold electrodes is described implicitly using self energies (see below).

B. Molecular-Dynamics Simulations and Semiempirical MO Theory

The underlying conformational sampling of the self-assembled monolayer systems investigated in this publication is based on classical atomistic molecular-dynamics simulations published and described in detail previously.¹¹ Here, the SAM-forming molecules were initially aligned on a clean (0001) aluminum-oxide surface that was equilibrated prior to depositing phosphonic acids using an interatomic potential model parameterized by Sun et al..¹⁷ The parameters for the phosphonates are based on the general Amber force field (GAFF)¹⁸ and the MD simulations were performed with the program DL-POLY.¹⁹ Details of the simulation are given in Ref. 11.

Following the MD simulations, an ensemble of snapshots was extracted and the AlO_x substrate was removed for further processing. The snapshot geometries were then treated by semiempirical MO calculations using the restricted Hartree-Fock formalism and the AM1 Hamiltonian.²⁰ All semiempirical MO calculations were performed using the parallel EMPIRE program.²¹

C. Model and Transport Theory

To study charge transport through the SAM, we use an effective single-particle model with parameters determined by the semiempirical MO calculations discussed above. Correspondingly, for a given snapshot of the structure of the SAM, the Hamiltonian of the SAM reads

$$H_S = \sum_j |\phi_j\rangle \epsilon_j \langle \phi_j|. \quad (1)$$

Thereby, ϵ_j denotes the energy of an electron in the j th MO $|\phi_j\rangle$.

Within the Landauer approach, transport through the SAM is described by the transmission function $t(E)$, which for an electron with energy E is given by²²

$$t(E) = \text{tr} \left\{ \Gamma_R G_S \Gamma_L G_S^\dagger \right\}. \quad (2)$$

Hereby, G_S denotes the retarded Green's function of the SAM,

$$G_S(E) = \left[E^+ - H_S - \Sigma_L(E) - \Sigma_R(E) \right]^{-1}, \quad (3)$$

which involves the self energies $\Sigma_\alpha(E)$ that describe the coupling of the SAM to the left and right electrodes ($\alpha = L, R$). The self energies are related to the width-function $\Gamma_\alpha(E)$, used in Eq. (2), via

$$\Sigma_\alpha(E) = \Delta_\alpha(E) - \frac{i}{2} \Gamma_\alpha(E), \quad (4)$$

where Δ_α denotes the level-shift function.

The calculation of the self energy requires explicit modeling of the gold electrodes and the gold-SAM interface.^{23,24} In this paper, we use a simpler strategy. We assume that the gold electrodes couple preferentially to selected carbon atoms of the C_{60} head groups at the left and right boundaries of the SAM. This choice is suggested by the geometrical structure of the SAM. Furthermore, we invoke the wide-band limit, where Γ_α can be approximated by a constant value and Δ_α vanishes. The wide-band limit is a good approximation for gold electrodes. Specifically, the matrix elements of the self energies $\Sigma_\alpha(E)$ in a local basis (represented by atomic orbitals $|\chi_\nu\rangle$) are given by

$$(\Sigma_\alpha(E))_{\nu\nu} = -\frac{i}{2} (\Gamma_\alpha)_{\nu\nu} \quad (5)$$

with $(\Gamma_\alpha)_{\nu\nu} = 1\text{eV}$ for orbitals ν corresponding to the outermost hexagon of Carbon atoms of the C_{60} head groups at the left and right boundary of the SAM and $(\Gamma_\alpha)_{\nu\nu'} = 0$ otherwise.

The value $(\Gamma_\alpha)_{\nu\nu} = 1$ eV represents a reasonable choice for molecule-gold contacts. It is emphasized that the results do not depend significantly on the exact value of this parameter, because the bottleneck for charge transport in the systems considered is the SAM itself and not the SAM-gold contact.

Based on the transmission function $t(E)$, the electrical current through the SAM is given by the expression

$$I(V) = \frac{2e}{h} \int dE t(E) (f_L(E) - f_R(E)), \quad (6)$$

where $f_{L/R}(E)$ denotes the Fermi function for the electrons in the left/right lead. It is given by

$$f_\alpha(E) = \frac{1}{1 + e^{(E - \mu_\alpha)/k_B T}} \quad (7)$$

with the Boltzmann constant k_B , the electrode temperature T and their chemical potentials μ_α ($\alpha = L, R$). For a symmetric voltage drop around the Fermi energy E_F , the chemical potentials are given by

$$\mu_\alpha = E_F \pm \frac{eV}{2}, \quad (8)$$

where V denotes the bias voltage. In the evaluation of the current, we assume that the transmission function $t(E)$ depends only weakly on the bias voltage and use its value at zero bias voltage.

It is noted that Landauer transport theory, as used here, can only describe coherent transport based on elastic scattering mechanisms. Dephasing and inelastic processes due to electron-phonon or electron-electron interaction are neglected. The study of these processes requires an extension of the model and more advanced transport methods, which will be the topic of future work. The influence of structural fluctuation will be considered in Sec. III E.

D. Analysis of Transport Pathways Using Local Currents

Eqs. (2) and (6) describe charge transport in terms of the overall electrical current and transmission function of the complete SAM. In order to have a more detailed description and, in particular, to analyze pathways of charge transport in the SAM, we use the method of local currents.^{25,26} As discussed in detail in Refs. 25 and 26, within this technique the overall current I through a surface perpendicular to the transport direction is represented

in terms of local currents via

$$I = \sum_{m \in M_L} \sum_{n \in M_R} I_{mn}, \quad (9)$$

where $M_{L/R}$ denotes atomic sites left and right of the chosen surface, respectively. As can be shown,^{15,26} the local contributions to the current from site n to m are given by

$$I_{mn} = \frac{2e}{h} \int \frac{dE}{2\pi} K_{mn}(E), \quad (10)$$

where

$$K_{mn}(E) = \sum_{\nu \in m} \sum_{\mu \in n} (V_{\nu\mu} G_{\mu\nu}^<(E) - V_{\mu\nu} G_{\nu\mu}^<(E)), \quad (11)$$

and

$$G^< = (if_L G_S \Gamma_L G_S^\dagger + if_R G_S \Gamma_R G_S^\dagger). \quad (12)$$

Thereby, we have used a representation in the local atomic orbital basis $|\chi_\nu\rangle$, where the Hamiltonian reads

$$H_S = \sum_{\mu} |\chi_\mu\rangle \tilde{\epsilon}_\mu \langle \chi_\mu| + \sum_{\mu \neq \nu} |\chi_\nu\rangle V_{\nu\mu} \langle \chi_\mu|. \quad (13)$$

Here, $\tilde{\epsilon}_\mu$ denotes the energy of an electron in orbital μ and $V_{\nu\mu}$ the coupling constant between orbitals ν and μ . For temperature $T = 0$, the expression $\sum_{m \in M_L} \sum_{n \in M_R} K_{mn}$ can be identified with the transmission function, Eq. (2), and thus K_{mn} defines local contributions to the transmission between pairs of atoms.

In the applications considered below, we use a further coarse graining, where the indices m and n in Eqs. (9 - 11) refer not to single atoms but to the C_{60} - C_{18} - or C_{10} -PA moieties in the SAM. Consequently, the sums in Eq. (11) also extend over the orbitals of all atoms of each C_{60} - C_{18} - or C_{10} -PA moiety. This allows a more straightforward analysis of the pathways of charge transport through the SAM.

III. RESULTS AND DISCUSSION

We have investigated three different SAM configurations as shown in Fig. 2, which differ both in the mixing ratio of C_{60} - C_{18} and C_{10} -PA groups and in their morphology. The basic unit representing the SAM is a cell consisting of 25 C_{60} - C_{18} PAs. Depending on the concentration of C_{10} -PA, the MD simulations reveal pronounced differences in the SAM morphologies. Fig. 2 (a) and (c) show snapshots of a 25:75 mixed SAM (containing, in addition,

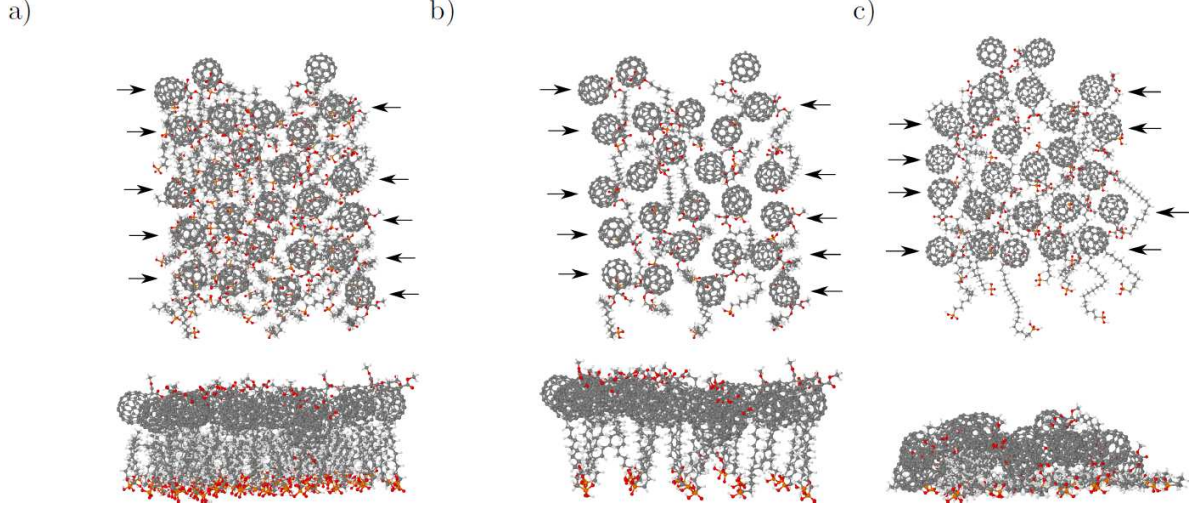


FIG. 2. Top- and sideview of SAM consisting of 25 C_{60} - C_{18} -PA (a) mixed with 75 C_{10} -PA after a MD simulation time of 50 ns (b) without the C_{10} -PA, but with identical geometry as shown in (a), (c) Pure 25 C_{60} - C_{18} -PA SAM morphology as derived from a different simulation.

75 C_{10} -PAs) and a pure SAM (without C_{10} -PAs), respectively, after a MD simulation time of 50 ns. The pure SAM exhibits a considerably reduced thickness and an enhanced disorder of the C_{60} head groups. Moreover, the C_{60} head groups are much closer to the surface in the pure SAM and, therefore, favor leakage currents into the substrate. Monte Carlo (MC) simulations and experiments have proven this morphology to be less conductive and have suggested a mixing ratio in the range of 25:75 – 50:50 to optimize the performance of the SAMFET devices.²⁷

In addition, we have considered the SAM depicted in Fig. 2 (b), which was obtained from the mixed SAM in panel (a) by removing the insulating C_{10} alkyl chains after the MD simulation. Although the geometrical structure of this system is artificial, it can give insight into the role the C_{10} -PA plays in the transport through the layer. Note that the realistic morphology of the pure SAM as derived from MD simulations is the one shown in (c).

A. Transport Properties and Molecular Orbital Analysis

We first consider the 25:75 SAM depicted in Fig. 2 (a). The energy spectrum of the MOs of this system in the range of $[-10, -2]$ eV is shown in Fig 3. The spectrum exhibits a dense distribution of energy levels and a HOMO-LUMO energy gap of 3.26 eV. In addition, the

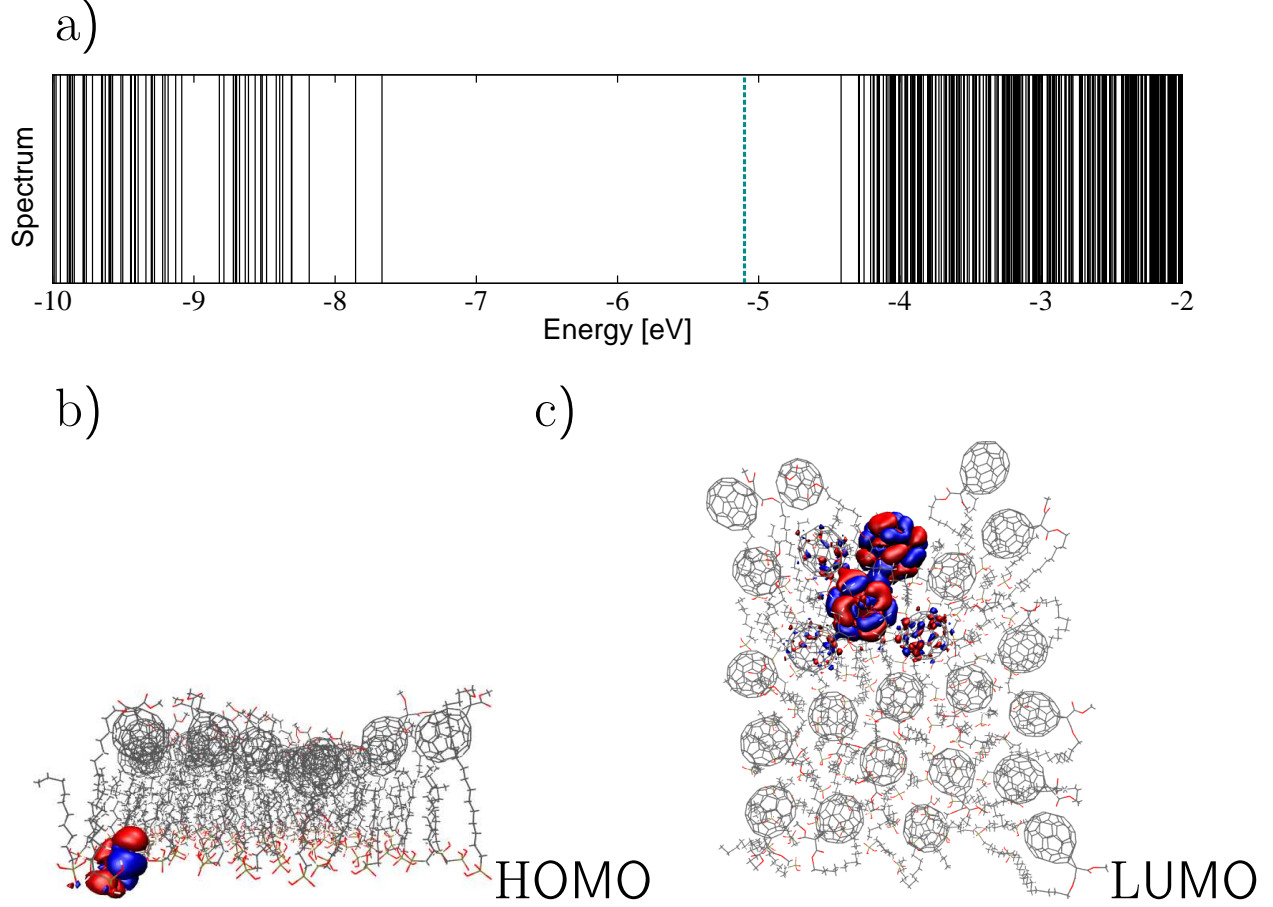


FIG. 3. Electronic structure of the 25:75 mixed SAM. (a) Energy levels shown as black lines. The blue dashed line denotes the Fermi level of gold used in the transport calculations ($E_F = -5.1$ eV). (b) highest occupied MO (c) lowest unoccupied MO. The MOs are plotted at isovalue $c = 0.001$.

HOMO and the LUMO of the SAM are depicted. Due to the pronounced structural disorder, all MOs are localized. The analysis reveals that the occupied orbitals close to the HOMO are mainly localized on the alkyl chains, while the unoccupied orbitals close to the LUMO are localized on the fullerenes. As fullerenes are electron conductors, only unoccupied energy states are relevant for transport processes. Therefore, in the simulations it is sufficient to take into account only the unoccupied part of the spectrum.

Fig. 4 shows the transmission function of the 25:75 SAM in an energy range close to the Fermi level (starting at E_{LUMO}). In addition, the energy levels are depicted as black lines. The transmission function exhibits a series of narrow peaks, which can be associated to individual energy levels of the molecular layer. The small widths of the peaks are due to the strong localization of the corresponding molecular orbitals, which results in a weak coupling

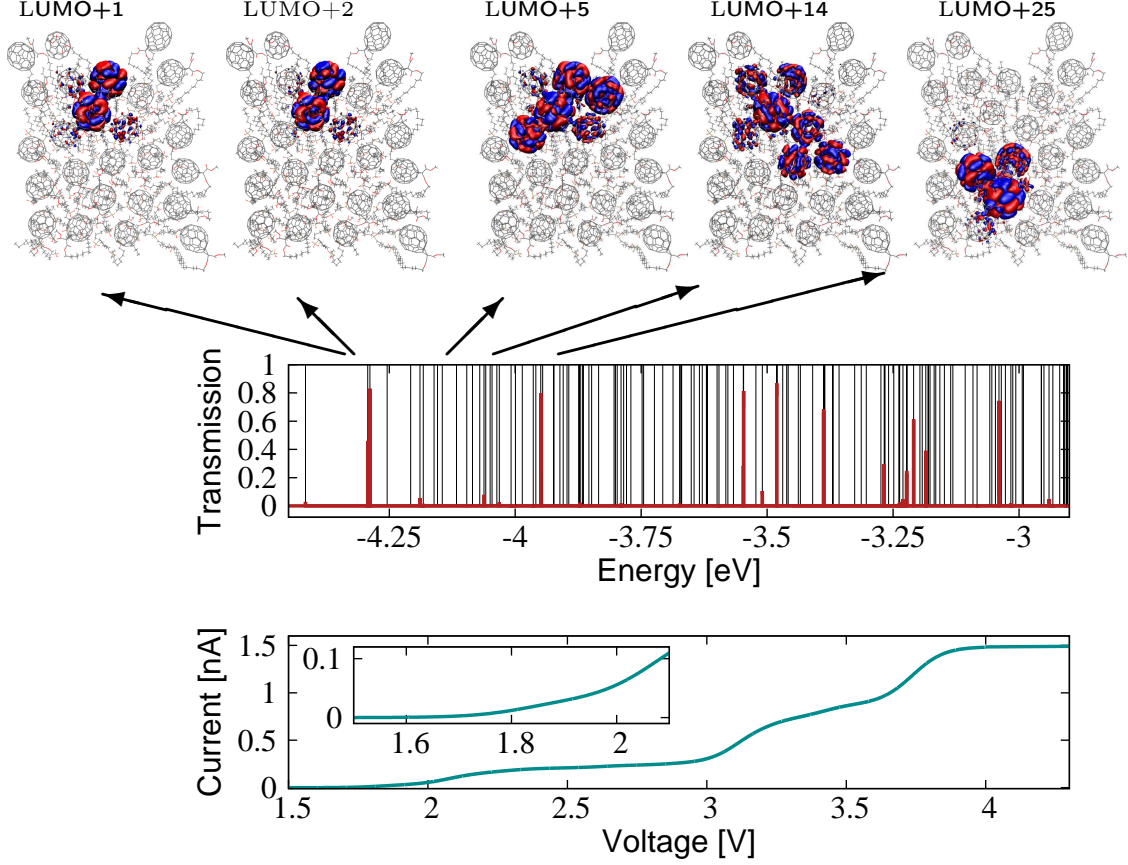


FIG. 4. Electronic structure and transport properties of the 25:75 mixed SAM Top: MO analysis, Center: Energy levels (black lines) and transmission function (red lines), Bottom: Current-voltage characteristic

to the electrodes. The current-voltage characteristic of the SAM at $T = 300$ K, depicted in Fig. 4 (bottom), shows a non-Ohmic behavior. Thermally broadened steps in the current appear at voltages, where the chemical potential of the left electrode, $\mu_L = E_F + eV/2$, is in resonance with energies E_i of the transmission peaks, i.e. at $V_i = 2|E_F - E_i|$.

As in the transmission function, the step structures in the current can be associated to contributions from individual MOs. For example, the rise of the current at $V \approx 1.65$ V is due to contributions of LUMO+1 and LUMO+2. Although their transmission values are comparably large, their contributions to the current are small because of the small widths of their transmission peaks. The step at $V \approx 1.82$ V corresponds to LUMO+5, which exhibits a small transmission coefficient of $t = 0.05$ but a much larger peak width. At larger voltages, we find the contributions of several higher unoccupied MOs. The overall magnitude of the current is on the order of nA , which is in agreement with experimental data.¹¹

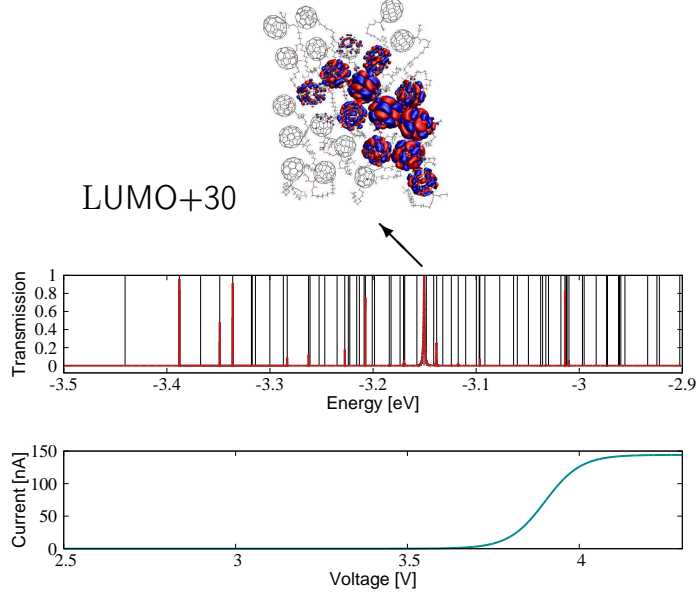


FIG. 5. Electronic structure and transport properties of the pure SAM with nonrelaxed geometry (see Fig. 2 (b)) Top: MO analysis, Center: Energy levels (black lines) and transmission function (red lines), Bottom: Corresponding current

B. Influence of Morphology and Mixing Ratio

In order to explore the influence of the morphology of the SAMs and the mixing ratio of the SAM-forming molecules on the transport properties, we consider the pure C_{60} - C_{18} -PA SAMs with the two different geometries shown in Fig. 2 (b) and (c). We first focus on the pure SAM with the unrelaxed geometry, which was obtained by removing the C_{10} -PAs groups from the 25:75 mixed SAM without further MD simulation. The transmission function and the current-voltage characteristic depicted in Fig. 5 reveal the pronounced influence of the C_{10} -PAs on the conductance properties of the SAMs. Compared to the mixed SAM, we find that the LUMO of the pure systems is shifted by almost 1 eV to higher energies. This and also a slight shift of the HOMO to lower values leads to an increase of the bandgap compared to the mixed SAM. Due to the larger bandgap, the onset of the current is shifted to higher voltages. However, the current magnitude is significantly larger than in the mixed SAM. The pronounced increase of the current at higher voltages ($V \approx 3.8$ V) can be related to transport through LUMO+30. As illustrated in Fig. 5 (top panel), LUMO+30 is a delocalized MO, which strongly couples to the electrodes resulting in a high current value of about 150 nA. Such delocalized MOs are not found in the mixed SAM. Thus, the

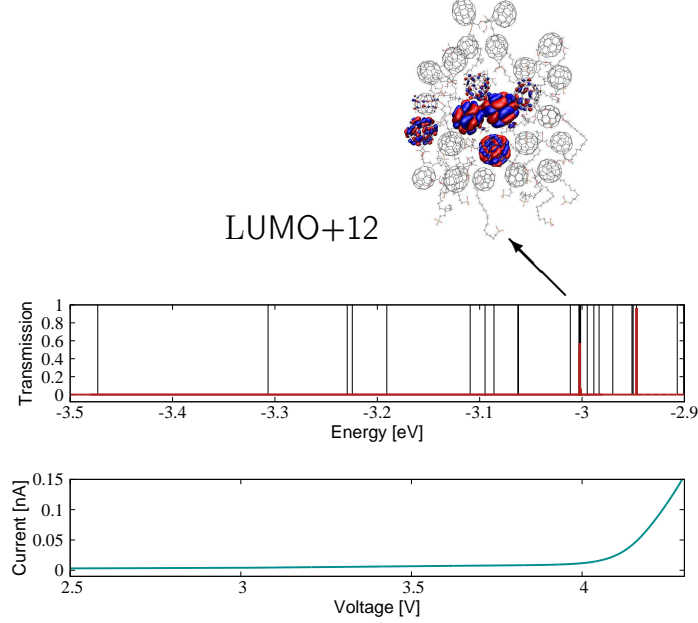


FIG. 6. Analysis of pure SAM (equilibrated) Top: MO analysis, Center: Energy levels (black lines) and transmission function (red lines), Bottom: Corresponding current

presence of the C_{10} -PAs in the mixed SAM appears to decrease the coupling between the fullerene head groups in the layer, which, in combination with the disorder of the layer, results in the more localized orbitals in the mixed SAM. Thus, in principle, the pure SAM with the geometry considered in Fig. 5 has (at least for higher voltages) better conductance properties than the mixed SAM. It should be noted, though, that this is only the case for the artificial geometry considered in Fig. 5. If the system is relaxed by further MD simulation, the morphology changes drastically to the geometry depicted in Fig. 2 (c), which will be considered next.

The electronic structure and conductance properties of the pure SAM with the morphology depicted in Fig. 2 (c) are shown in Fig. 6. The results reveal that the almost flat and strongly disordered morphology modifies the electronic structure profoundly and results in a very small current, which confirms conclusions from previous simulations and experiments.¹¹ Evidently, due to the disorder, the C_{60} head groups in the layer cannot form a conductive channel. The contributing MOs are strongly localized, leading to narrow peak structures in the transmission function. Also, we find a shift of the LUMO to higher energies. The current onset is located at high voltages and has values about one order of magnitude smaller than for the mixed SAM. These findings show that the poor conduction properties

of pure C_{60} - C_{18} -PA SAMs can clearly be related to the decreased order in the molecular structure. Additionally, when used in SAMFETs, higher leakage currents can appear due to the smaller distance of the fullerenes to the substrate, as was indeed found in the transport measurements^{28,29}.

C. Pathways for Electron Transport

So far, we have analyzed the conductance properties of the SAMs in terms of the overall transmission function and currents. To obtain a more detailed understanding of the transport properties and mechanisms, we analyze the local pathways for electron transport through the SAM. Previous investigations using Monte Carlo path searches based on a local electron affinity potential in the mixed SAM have suggested that there are specific pathways for efficient electron transport across the fullerenes.¹¹ In the following we will extend this analysis based on the quantum mechanical transport theory employed here using the theory of local currents and transmissions outlined in Sec. IID.

We first consider the local transmission, defined by Eq. (11). Test calculations show that contributions from the insulating C_{10} -PA groups, e.g. from C_{10} -PA to C_{60} - C_{18} -PA or between pairs of C_{10} -PAs, are very small. Therefore, we restrict the discussions to local contributions only between C_{60} -containing molecules. The local transmissions were calculated at the energies E , where the total transmission (cf. Fig. 4) exhibits its maxima. Each of these maxima can be related to a single MO in the spectrum. The results for energies $E_{\text{LUMO}+2}$ (with a total transmission of $t = 0.79$) and $E_{\text{LUMO}+25}$ ($t = 0.69$) are shown in Fig. 7. In the plots, local transmissions between all C_{60} - C_{18} -PA molecules are depicted as arrows. The color code ranging from blue to orange indicates the local transmission value. An arrow is only drawn when this value exceeds 0.01. In this manner, a pathway for the electron through the monolayer can be visualized. The shape of the pathway can clearly be related to the shape of the corresponding MO as shown, e.g. in Fig. 7 (a,b) for LUMO+2. The non-vanishing local transmission components are mainly located on molecules which exhibit significant MO density. This is also illustrated for the transmission path at energy $E_{\text{LUMO}+25}$ in Fig. 7 (e,f).

By integrating the local transmissions over energy, the local current is obtained, see Eq. (10). This corresponds to a weighted sum of all local transmission paths contributing at

a certain voltage. Tuning the bias voltage, the number of energy levels within the bias window and thus the number of possible transport channels is increased. By plotting the local current components, we can visualize all channels which are open at a specific voltage. Fig. 8 shows the local currents at a bias voltage of $V = 2.4$ V. The local currents are represented as arrows between pairs of C_{60} - C_{18} PAs, where the color of the arrows indicates the strength of the current. An arrow is only drawn if the current is larger than 0.01 nA. At the voltage considered, several transmission channels contribute. The dominating electron path corresponds to the contribution of LUMO+25 (cf. Fig. 7 (e,f)). In the upper region of the SAM, smaller contributions of the lower unoccupied orbitals (especially LUMO+2,+5,+14, cf. Fig. 7 (a)) are seen. There are also crossing components of the local currents between the different regions. The pathways obtained based on the local current calculations are compared in Fig. 8 to the results of MC paths searches (yellow colored density) performed using the local electron affinity energy map^{11,30} of the system. In the MC simulation, paths were initialized at the left boundary of the SAM such that they can start at all five outermost C_{60} groups in agreement with the contact scenario used in the local current calculation. In the MC simulation a temperature of $T = 2500$ K is used. Computationally this temperature can be attributed to the acceptance rate of the MC steps and physically it is related to a higher thermal energy of the electrons (285 meV) experimentally supplied by the operation voltage of the devices. We find that the channels of high local currents agree well with the MC results. There are some minor deviations. For example, the MC simulation misses the currents that cross between different regions. On the other hand, the MC simulation may also find paths localized in between the molecules, which are by definition not present in the local current that describes transitions between molecules. The overall rather good agreement of the results obtained by two quite different approaches supports the robustness of the results.

D. Influence of Electrode-SAM Contact Geometry

We have, furthermore, investigated the influence of the electrode-SAM contact geometry on the local transmission paths and the overall current. This was achieved by varying the self energy (cf. Sec. II C), which allows the C_{60} head groups to which the electrodes couple to be selected. The influence of the contact scenario on transport is illustrated in Fig. 7 for the

local transmission at energy $E_{\text{LUMO}+2}$. The results show that the starting and end points of the pathways depend strongly on the C_{60} head group the electrodes couple to. For example, in Fig. 7 (c) and (d), where a smaller number of C_{60} were contacted, the transmission values are significantly reduced. Moreover we find that the transmission is strongly decreased if the electrodes couple only to molecules far away from those with MO density.

The total current obtained for the three different contact scenarios depicted in Fig. 7 (a, c, d) is shown in Fig. 9. At larger voltages, where many transmission channels contribute, the overall current scales linearly with the number of molecules contacted. However, at smaller voltages this is not the case. For example, the current obtained for contact to only a single fullerene (cf. Fig. 7 (d)) is larger than that for the scenario of Fig. 7 (c) with three fullerenes in contact. This shows that for smaller voltage, the number of contributing channels and thus the current magnitude depends sensitively on the specific electrode-molecule contact scenario.

E. Influence of Structural Fluctuations

All results discussed so far were obtained for a SAM with fixed geometry, i.e. a single snapshot taken at a fixed time of the MD simulation. However, structural fluctuations may play an important role for transport processes in the SAM. For instance, the formation of conductive pathways depends critically on the molecular arrangement, e.g. on the distance between the fullerene head groups.

To study the importance of structural fluctuations, we have analyzed the electronic structure and the transport properties for several snapshots taken at different times along a MD trajectory. Fig. 10 shows the energy spectrum, the transmission function and the current-voltage characteristic for three representative examples, taken at $t = 16$ ns, $t = 25$ ns and $t = 44.25$ ns. The comparison of the spectra for the different geometries reveals significant fluctuations of the energy levels. The energy of the LUMO, for example, fluctuates by about 0.1 eV. As a result, the transmission functions change significantly, which, in turn, results in fluctuations of the current by about one order of magnitude. These examples show that structural fluctuations can influence the electronic structure and the transport properties in the C_{60} -SAMs significantly.

A more detailed analysis of the influence of fluctuations on the transport properties

requires, in principle, a theoretical treatment beyond the methodology employed here, using, e.g. time-dependent density matrix or nonequilibrium Green’s function (NEGF) methods.³¹ This will be the the subject of future work.

IV. CONCLUSIONS

We have investigated charge transport in C_{60} -based SAMs, which are used in SAMFET devices. The theoretical study was based on a combination of MD simulations to characterize the structure of the SAMs, semiempirical MO electronic structure calculation and Landauer transport theory.

The analysis shows that the transport characteristics can be related to the structural and electronic properties of the SAMs. Due to the structural disorder of the SAMs, the molecular orbitals are predominantly localized. As a result, the transmission characteristics are dominated by narrow peaks, which can be assigned to the specific molecular orbitals, and give rise to relatively low levels of electrical current, in qualitative agreement with experiment. A comparison of SAMs with different mixing ratios of C_{60} and alkene groups revealed, furthermore, the strong dependence of the transport properties on the layer composition. The conductivity depends crucially on the formation of conductive transport channels across the C_{60} head groups, which requires a certain degree of order. Extending previous work,^{11,13} our studies show that mixing C_{60} - C_{18} -PAs with C_{10} -PA increases the molecular order and facilitates transport. In SAMs consisting of pure C_{60} - C_{18} -PAs, on the other hand, the disordered molecular structure hinders the formation of conduction channels and results in a poor performance.

We have also analyzed pathways of charge transport in the SAMs employing the theory of local currents. The results demonstrate that the electrical current is dominated by few selected pathways, which facilitate transport through the SAM. The specific contact scenario to the electrodes may influence the selection of pathways, and thus affect the level of the electrical current.

Another important aspect of transport in organic SAMs is the effect of structural fluctuation on the transport properties. Our results show that although the structural fluctuations within the SAM are relatively small, they have a significant effect on the transport properties and result in fluctuations of the current by about an order of magnitude. This is especially

due to fluctuations in the alignment of the fullerenes. To further examine the role of fluctuations on the transport properties, a time-dependent treatment of charge transport^{32,33} is required, using, e.g., time-dependent nonequilibrium Green's function (NEGF) theory.³⁴ This may also open the door to a more complete theoretical treatment, including inelastic processes due to electron-electron and electron-phonon interaction.

ACKNOWLEDGMENTS

This work was supported by the the Deutsche Forschungsgemeinschaft (DFG) through the Cluster of Excellence 'Engineering of Advanced Materials' (EAM) and SFB 953. Generous allocation of computing time at the computing centers in Erlangen (RRZE), Munich (LRZ), and Jülich (JSC) is gratefully acknowledged.

REFERENCES

- ¹T. Sekitani, T. Yokota, U. Zschieschang, H. Klauk, S. Bauer, K. Takeuchi, M. Takamiya, T. Sakurai, and T. Someya, *Science* **326**, 1516 (2009).
- ²T. Sekitani, U. Zschieschang, H. Klauk, and T. Someya, *Nat. Mater.* **9**, 1015 (2010).
- ³C. Tanase, E. J. Meijer, P. W. M. Blom, and D. M. de Leeuw, *Org. Electron.* **4**, 33 (2003).
- ⁴M. Mottaghi and G. Horowitz, *Org. Electron.* **7**, 528 (2006).
- ⁵J. J. Brondijk, W. S. C. Roelofs, S. G. J. Mathijssen, A. Shehu, T. Cramer, F. Biscarini, P. W. M. Blom, and D. M. de Leeuw, *Phys. Rev. Lett.* **109**, 056601 (2012).
- ⁶E. C. P. Smits, S. G. J. Mathijssen, P. A. van Hal, S. Setayesh, T. C. T. Geuns, K. A. H. A. Mutsaers, E. Cantatore, H. J. Wondergem, O. Werzer, and R. Resel, *Nature* **455**, 956 (2008).
- ⁷T. Schmaltz, A. Y. Amin, A. Khassanov, T. Meyer-Friedrichsen, H.-G. Steinrck, A. Magerl, J. J. Segura, K. Voitchovsky, F. F. Stellacci, and M. Halik, *Adv. Mater.* **5**, 4511 (2013).
- ⁸H. Klauk, U. Zschieschang, J. Pflaum, and M. Halik, *Nature* **445**, 745748 (2007).
- ⁹M. Novak, A. Ebel, T. Meyer-Friedrichsen, A. Jedaa, B. F. Vieweg, G. Yang, K. Voitchovsky, F. Stellacci, E. Spiecker, and A. Hirsch, *Nano Lett.* **11**, 156 (2010).
- ¹⁰A. Ringk, X. Li, F. Gholamrezaie, E. C. P. Smits, A. Neuhold, A. Moser, C. Van der Marel, G. H. Gelinck, R. Resel, D. M. de Leeuw, and P. Strohriegel, *Adv. Funct. Mater.*

- 23**, 2016 (2012).
- ¹¹C. M. Jäger, T. Schmaltz, M. Novak, A. Khassanov, A. Vorobiev, M. Hennemann, A. Krause, H. Dietrich, D. Zahn, A. Hirsch, M. Halik, and T. Clark, J. Am. Chem. Soc. **135**, 4893 (2013), <http://pubs.acs.org/doi/pdf/10.1021/ja401320n>.
 - ¹²T. Stubhan, M. Salinas, A. Ebel, F. C. Krebs, A. Hirsch, M. Halik, and C. J. Brabec, Adv. Energy Mater. **102**, 532 (2012).
 - ¹³M. Novak, T. Schmaltz, H. Faber, and M. Halik, Appl. Phys. Lett. **98**, 093302 (2011).
 - ¹⁴R. Landauer, IBM J. Res. Dev. **1**, 223 (1957).
 - ¹⁵A. Pecchia and A. D. Carlo, Rep. Prog. Phys. **67**, 1497 (2004).
 - ¹⁶T. Bauer, T. Schmaltz, T. Lenz, M. Halik, B. Meyer, and T. Clark, ACS Appl. Mater. Interfaces **5**, 60736080 (2013).
 - ¹⁷J. Sun, T. Stirner, W. E. Hagston, A. Leyland, and A. Matthews, J. Cryst. Growth **290**, 235 (2006).
 - ¹⁸J. Wang, R. M. Wolf, J. W. Caldwell, P. A. Kollman, and D. A. Case, J. Comput. Chem. **25**, 1157 (2004).
 - ¹⁹I. T. Todorov, W. Smith, K. Trachenko, and M. T. Dove, J. Mater. Chem. **16**, 1911 (2006).
 - ²⁰M. J. S. Dewar, E. G. Zoebisch, E. F. Healy, and J. J. P. Stewart, J. Am. Chem. Soc. **107**, 3902 (1985).
 - ²¹M. Hennemann and T. Clark, *EMPIRE* (Universität Erlangen-Nürnberg, 2012) <http://www.ceposinsilico.de/products/empire.htm>.
 - ²²S. Datta, *Electronic Transport in Mesoscopic Systems* (Cambridge University Press: New York, 1997).
 - ²³C. Benesch, M. Cizek, J. Klimes, M. Thoss, and W. Domcke, J. Phys. Chem. C **112**, 9880 (2008).
 - ²⁴J. C. Cuevas and E. Scheer, *Molecular Electronics: An Introduction To Theory And Experiment* (World Scientific, Singapore, 2010).
 - ²⁵T. N. Todorov, J. Phys.: Condens. Matter **14**, 3049 (2002).
 - ²⁶G. C. Solomon, C. Herrmann, T. Hansen, V. Mujica, and M. A. Ratner, Nat Chem **2**, 223 (2010).
 - ²⁷A. Rumpel, M. Novak, J. Walter, B. Braunschweig, M. Halik, and W. Peukert, Langmuir **27**, 15016 (2011).

- ²⁸M. Burkhardt, A. Jedaa, M. Novak, A. Ebel, K. Votchovsky, F. Stellacci, A. Hirsch, and M. Halik, *Adv. Mater.* **22**, 2525 (2010).
- ²⁹A. Jedaa, M. Salinas, C. M. Jger, T. Clark, A. Ebel, A. Hirsch, and M. Halik, *Appl. Phys. Lett.* **100**, 063302 (2012).
- ³⁰T. Clark, *J. Mol. Model* **16**, 1231 (2010).
- ³¹G. Stefanucci and R. van Leeuwen, *Nonequilibrium Many-Body Theory of Quantum Systems* (Cambridge University Press: New York, 2013).
- ³²P. B. Woiczikowski, T. Kubar, R. Gutierrez, R. A. Caetano, G. Cuniberti, and M. Elstner, *J. Chem. Phys.* **130**, 215104 (2009).
- ³³A. Croy and U. Saalmann, *Phys. Rev. B* **80**, 245311 (2009).
- ³⁴B. Popescu, P. B. Woiczikowski, M. Elstner, and U. Kleinekathöfer, *Phys. Rev. Lett.* **109**, 176802 (2012).

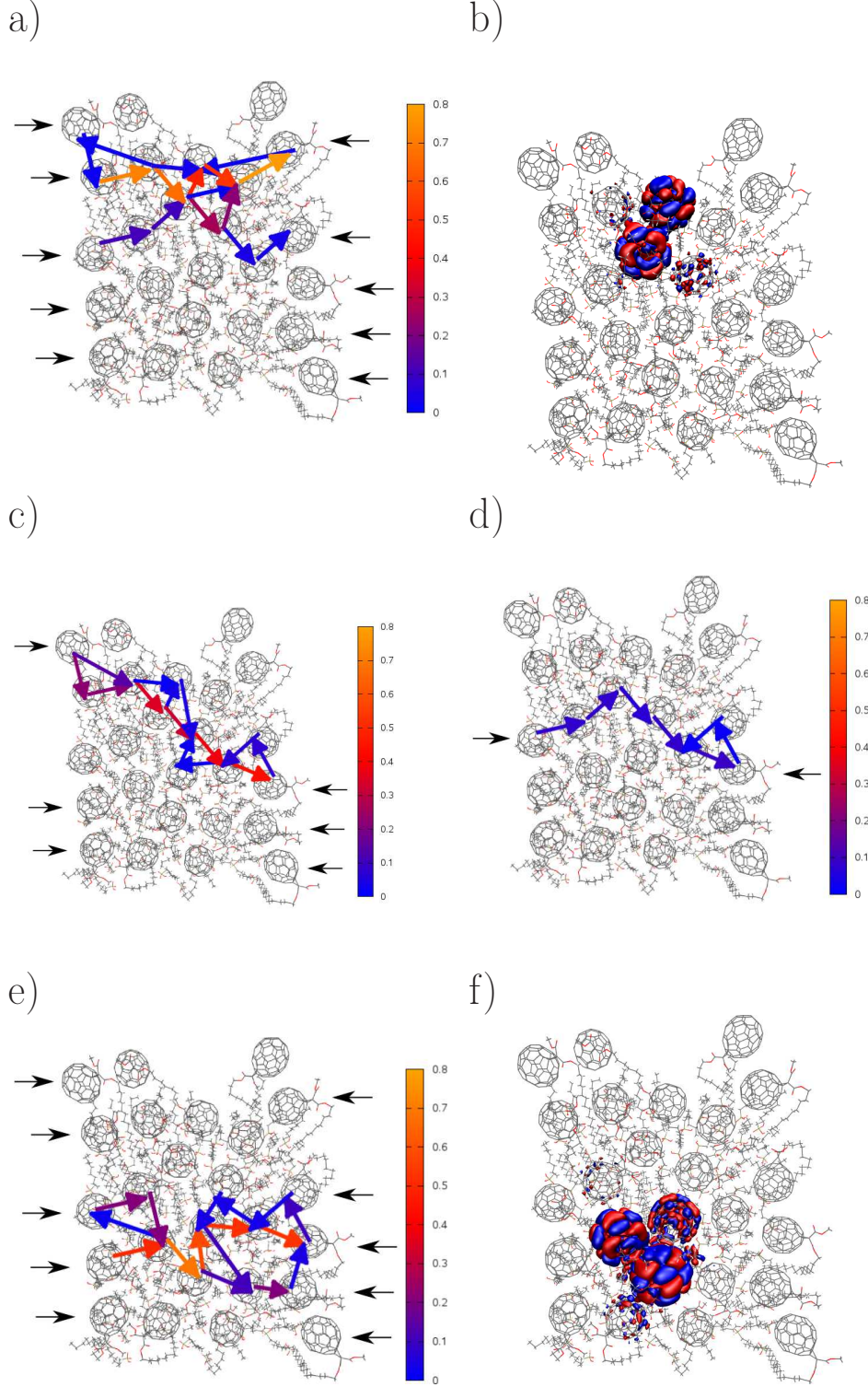


FIG. 7. Local transmissions between pairs of C_{60} - C_{18} -PAs and their relation to the MO structure. The colors of the arrows are ordered from blue to orange referring to an increasing transmission amplitude from 0 to 0.8. Black arrows indicate the C_{60} groups contacted by the electrodes. (a,c,d) Local transmissions at E_{LUMO+2} for different contact scenarios, (b) LUMO+2, (e) Local transmissions at $E_{LUMO+25}$, (f) LUMO+25

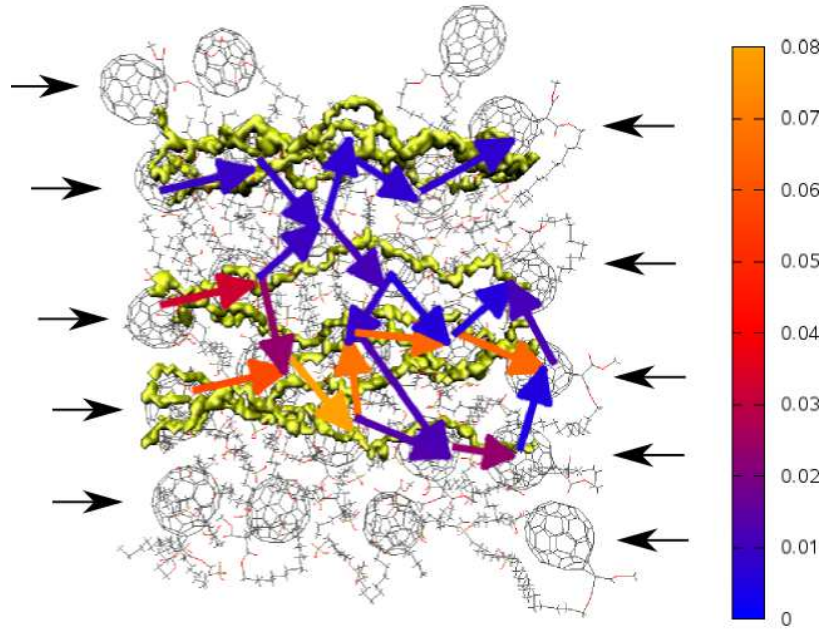


FIG. 8. Local currents at $V = 2.4$ V (scale from blue to orange in nA) compared to MC transfer paths through the mixed SAM. The MC paths are shown as underlying yellow paths and were calculated at $T = 2500$ K.

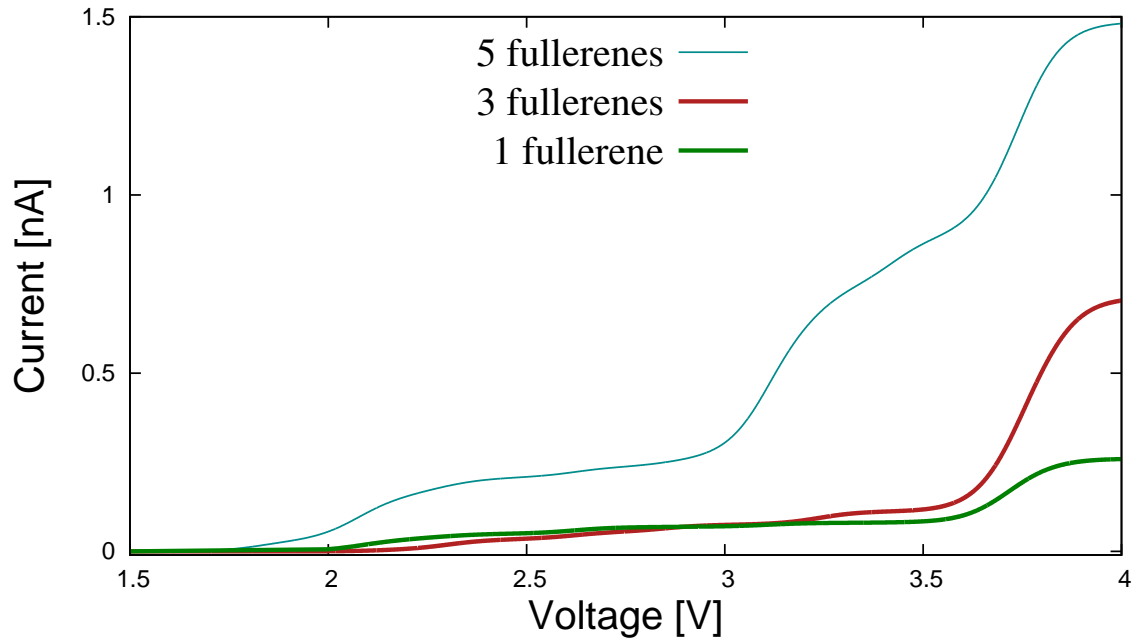


FIG. 9. Comparison of currents for the different contact scenarios depicted in Fig. 7 (a, c, d)

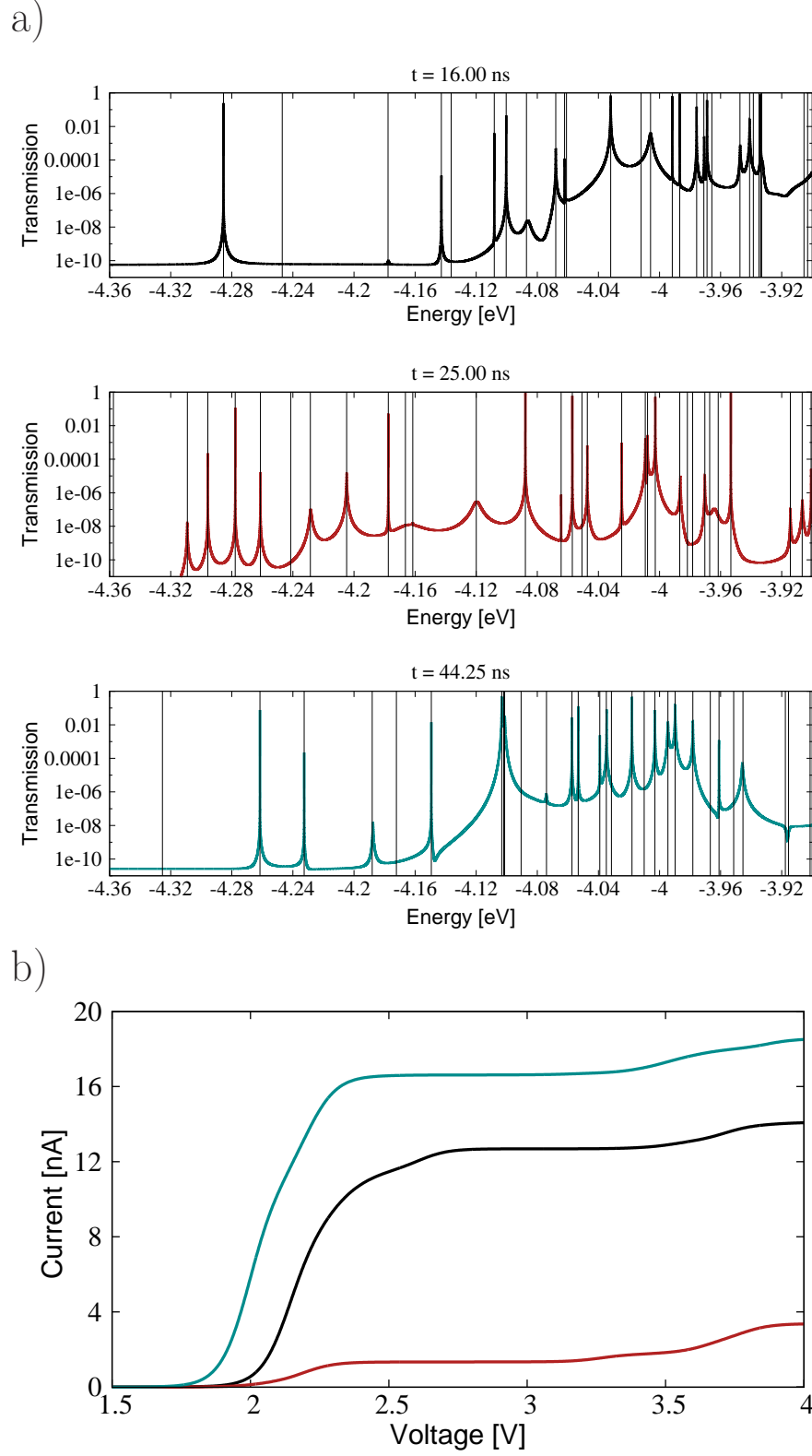


FIG. 10. Energy level spectrum, transmission function (a) and current-voltage characteristic (b) for different geometries of the SAM taken at three different times of the MD simulation.